Heat Transport at the Boundary of ASDEX Upgrade

C S Pitcher, A Herrmann, H Murmann,
H Reimerdes, J Schweinzer, W Suttrop, H Salzmann
and the ASDEX Upgrade Team and NBI Team

IPP 1/295 Januar 1997

MAX-PLANCK-INSTITUT FÜR PLASMAPHYSIK

85748 GARCHING BEI MÜNCHEN

MAX-PLANCK-INSTITUT FÜR PLASMAPHYSIK

GARCHING BEI MÜNCHEN

Heat Transport at the Boundary of ASDEX Upgrade

C S Pitcher, A Herrmann, H Murmann,
H Reimerdes, J Schweinzer, W Suttrop, H Salzmann
and the ASDEX Upgrade Team and NBI Team

IPP 1/295 Januar 1997

Die nachstehende Arbeit wurde im Rahmen des Vertrages zwischen dem Max-Planck-Institut für Plasmaphysik und der Europäischen Atomgemeinschaft über die Zusammenarbeit auf dem Gebiete der Plasmaphysik durchgeführt.

For Submission to 'Plasma Physics and Controlled Fusion'

Heat Transport at the Boundary of ASDEX Upgrade

C S Pitcher†, A Herrmann, H Murmann, H Reimerdes
J Schweinzer, W Suttrop, H Salzmann
and the ASDEX Upgrade Team and NBI Group

Max-Planck-Institut für Plasmaphysik, IPP-EURATOM Association, Garching and Berlin, Germany

†MIT Plasma Fusion Center, Cambridge, Massachusetts 02139, USA

January 17, 1997

Abstract

The flow of heat in the scrape-off layer region of ASDEX Upgrade is investigated and compared with simple modelling. Parallel heat transport is found to be consistent with electron heat conduction based on Spitzer-Härm conductivity. Cross-field heat transport is characterized using radial e-folding distances for power, temperature and plasma pressure, which are all found to vary weakly over a wide range of discharge conditions. Type I ELMs, also characterized, introduce a discreteness to the power flow into the SOL and carry approximately half of the power exhaust from the discharge. The divertor plates are effectively screened from the ELM energy, even in low radiation discharges, suggesting enhanced radiation rates during ELMs.

1 Introduction

The most critical issue with respect to divertor operation in tokamak reactors, e.g. ITER [1], is the transport of heat in the boundary region, and particularly, the scrape-off layer (SOL). For a given alpha-heating power, this determines the power density incident on divertor plate structures, or, alternatively, the required divertor radiation density in dissipative scenarios, such as those presently envisaged [1]. While other aspects of the divertor, e.g. helium exhaust, impurity production and retention, etc., will affect the reactor efficiency, the power density flowing to the plates has the potential to seriously jeopardize the mac hardware, possibly preventing continued operation.

There are a large number of outstanding and detailed issues related to the flow of power in the SOL of divertor tokamaks. In particular, an understanding, or at least characterization, of the processes which determine the parallel power e-folding distance in the SOL is required, i.e. λ_P. We define λ_P (as well as other characteristic widths) to be the value at the outside mid-plane. λ_P is determined by the relative rates of cross-field transport into the SOL from the main plasma, compared with the parallel exhaust rate to the divertor. In the case of the (anomalous) cross-field transport, in this paper, we simply characterize the observed radial widths as directly determined by infra-red thermography at the plates, and as inferred from measurements of the electron temperature and pressure e-folding widths upstream of the divertor, λ_T and λ_{pr}, respectively. The inferred values are derived using simple analytic models presented in Sects. 2 and 3. We discuss circumstances when λ_P, as inferred at the plate, is not a good measure of the power width outside of the divertor (i.e. cases with high divertor radiation). In the case of the parallel transport of heat in the SOL, we quantitatively compare the observed behaviour with predictions based on Spitzer-Härm conductivity.

In H-mode discharges, in addition to the above, the power flow in the SOL is partly determined by small MHD events, edge localized modes (ELMs) [2], which introduce a discreteness into the power exhaust, both for the cross-field transport and the parallel transport. We characterize the ELM transport of heat in Type I ELMy discharges. The measurements presented here are taken from the ASDEX Upgrade tokamak.

2 Two-Point Model

At this point we introduce a simple one-dimensional model, often called the 'Two-Point' model, based on parallel electron heat conduction and pressure balance, forms of which have been employed by numerous authors and is summarized in a recent review [3]. We briefly restate the basic results here, providing a framework for the experimental data presented later.

In this paper we concentrate on the first power e-folding distance, immediately adjacent to the last closed flux surface (LCFS), since this is the most critical of regions with respect to divertor power handling. We assume that the parallel exhaust of power from the SOL to the divertor is due to electron heat conduction. The parallel power density q is therefore governed by the heat conduction equation according to Spitzer-Härm [4],

$$q = -\kappa_0 T^{5/2} \frac{dT}{dx} \tag{1}$$

where κ_0 is a constant and x is the distance along the field line ($x = 0$ at the stagnation point or upstream location, $x = L$ at the plate). We assume that

$T_i = T_e$. If Eqn. 1 is integrated from the upstream location 'u' to the target plate 't', we arrive at,

$$T_u^{7/2} - T_t^{7/2} \simeq \frac{7 q_u L}{2\kappa_0} \tag{2}$$

where we have assumed that the parallel power is approximately constant over most of the length of the flux tube. This is approximately valid even in cases with high radiation on open surfaces, since such radiation tends to be localized near the divertor where densities are usually elevated.

We consider here only the case of a cold divertor, i.e. where $T_u \gg T_t$, and thus Eqn. 2 becomes,

$$T_u \simeq \left(\frac{7 q_u L}{2\kappa_0}\right)^{2/7} \tag{3}$$

One sees from Eqn. 3 that the upstream temperature is independent of the divertor conditions and depends only weakly on the upstream power density q_u and the connection length L. Also from Eqn. 3, if one assumes an exponential radial dependence for q and T, the power e-folding distance λ_P can be immediately related to the temperature e-folding distance λ_T,

$$\frac{\lambda_P}{\lambda_T} = \frac{2}{7} \tag{4}$$

3 Relation Between Pressure and Power Profiles

While it may seem intuitive that the radial profiles in the SOL of plasma pressure and parallel power flow may be related, the relationship is not immediately clear. In this section we derive an approximate relation between the two, based on balances between the source of power, i.e. parallel conduction along field lines, and the two possible sinks near the divertor, i.e. direct deposition on the divertor plate or volume radiative processes close by [3, 5].

First, we consider the case where radiation levels are low, pressure is conserved along each flux tube and most of the upstream parallel power reaches the divertor target plate, i.e. $q_u \approx q_t$. The boundary condition at the target surface requires,

$$q_u \approx q_t = n_t c_{St} \gamma T_t = \frac{c_{St}\gamma}{4} p_u \tag{5}$$

where $\gamma = 7$ is the sheath transmission factor [6] , c_{St} is the ion acoustic speed at the target and p_u is the total upstream pressure (ion + electron), where we have taken into account a factor of two increase in static pressure at the upstream location over the target plate value [6]. For most conditions of interest, where $T_t \ll T_u$, it turns out from modelling [5] and experimental results [7] that T_t has only a weak dependence on radial location, and thus $c_{St} \propto T_t^{1/2}$ is approximately constant with

radius. Thus, we are left with an approximate relation, $q_u \propto p_u$, i.e. the radial profiles of parallel power and plasma pressure should be approximately similar.

Next we consider the other extreme case, where no power reaches the plate and the upstream power flow is completely radiated near the divertor by impurities [3]. The volumetric loss of parallel power by impurity radiation (we neglect hydrogenic radiation) is given by,

$$\frac{dq}{dx} = -c_z n^2 L_z \tag{6}$$

where c_z is the impurity concentration, n is the plasma density and L_z is the radiated power coefficient. Combining Eqns. 1 and 6, integrating from the upstream point to the target plate and assuming $T_t \ll T_u$ we arrive at,

$$q_u^2 \approx \frac{1}{3}\kappa_0 c_z L_z p_u^2 T_u^{3/2} \tag{7}$$

We have assumed that radiation loss by impurities occurs upstream of the recycling region, and specifically upstream of the frictional zone, which would probably exist at very low plasma temperatures near the plate under highly radiative conditions. We assume that the impurity concentration c_z and radiated power coefficient L_z are constant along the flux tube. Finally, if we use Eqn. 3 for T_u, one arrives at $q_u \propto p_u^{14/11} \approx p_u$, the same approximate scaling as in the low radiation case. Thus, in both regimes the pressure and parallel power profiles should be approximately similar, i.e. $\lambda_P \approx \lambda_{pr}$, where λ_{pr} is the characteristic width of the pressure profile near the separatrix.

This conclusion is arrived at using several assumptions, some of them questionable, particularly the assumptions of constant c_z and L_z along field lines which lead to Eqn. 7. It is not implied that this simple derivation is rigorously adhered to. Instead, the pressure width λ_{pr} is to be used simply as an 'indication' of the power width λ_P, in cases where λ_P cannot be directly measured by other means.

4 Experimental Details

The ASDEX Upgrade tokamak (AUG), Fig. 1, is a single-null divertor machine, with graphite as the primary first-wall material and neutral beam injection (NBI) heating up to $P_{NBI} \approx 10MW$ [8]. The plasma boundary is extensively diagnosed. Specifically in this paper we use data from a moving 'In-Vessel' Langmuir probe (IVP), which scans approximately $10cm$ above the outer divertor plate providing plasma n_e and T_e profiles [9], infra-red thermography at the plates giving the power density distribution q_t [10], high resolution electron cyclotron emission (ECE) at the outside mid-plane for T_u profiles [11] and a lithium beam, also at the outside mid-plane, for n_u profiles [12]. In addition, Thomson scattering is used, which can either provide high resolution profiles of n_e and T_e of the plasma boundary at the

outside mid-plane or, alternatively, in the core region [13]. Although the spatial separation of the channels of the core Thomson system is relatively large, $\approx 2cm$, the measurement has relatively high spatial accuracy near the boundary owing to the expanded flux surfaces at the point of measurement, Fig. 1.

The use of ECE to diagnose the plasma boundary, and particularly the SOL, is relatively new. For the geometry and magnetic field of ASDEX Upgrade, an optical depth of $\tau = 3$, needed for 95% black-body intensity with single pass absorption, requires $n_e \times T_e = 1.2 \times 10^{19} keVm^{-3}$. However, it is found experimentally from comparison with Thomson scattering [14], that agreement to within 15% is obtained down to $n_e \times T_e = 3.0 \times 10^{18} keVm^{-3}$. This is consistent with multiple pass absorption with a wall reflectivity of 65%, which has also been independently measured in the laboratory for the graphite tiles of ASDEX Upgrade. Only ECE edge data with $n_e \times T_e$ values above this are used in the present paper. Also, as discussed in [14], under conditions of high heating power and high edge gradient of T_e, in particular during some Type I ELMy H-modes, non-thermal enhanced cyclotron radiation appears at the plasma boundary. This phenomenon leads to radiation temperatures exceeding the true electron temperature and therefore such conditions are excluded in these results.

Fig. 2 gives typical profiles of electron density, temperature, pressure and parallel power from two identical H-mode discharges with $I_p = 1.0MA$,$B_t = 2.5T$, $\overline{n}_e = 8 \times 10^{19} m^{-3}$ and $P_{NBI} = 5.0MW$. All measurements are mapped to the outside midplane with an absolute accuracy of $\approx 1cm$, and a relative accuracy of $\approx 1mm$. The radiation level was modest in these discharges, i.e. $P_{rad} \approx 2MW$. Fig. 2a includes density measurements from the core and edge Thomson systems and the lithium beam. Fig. 2b gives T_e measurements from the two Thomson systems. Fig. 2c gives the electron pressure p_e profile derived from the two Thomson systems. Fig. 2d gives the parallel power profile q_t obtained with IR thermography at the outer plate.

In general, good agreement is obtained between the various diagnostics, allowing for the $\approx 1cm$ absolute positional uncertainty. One exception is the separatrix density as obtained with the core Thomson system, which is approximately a factor of two higher than the edge Thomson and the lithium beam, although good agreement with the edge Thomson is obtained in the case of T_e. This discrepancy is ascribed to the difficulty of maintaining the absolute calibration of the Thomson scattering system when shifting the laser beam, the collection optics and the detection system between the edge and core measuring locations.

The parallel power profile, Fig. 2d, is significantly narrower than the corresponding n_e and T_e profiles, i.e. $\lambda_P \approx 5mm$ compared with $\lambda_n \approx 25mm$ and $\lambda_T \approx 13mm$, but is comparable to the pressure width $\lambda_{pr} \approx 7mm$. These relative widths are consistent with the results of Sect. 2, i.e. that parallel power flow is due to parallel electron heat conduction, the subject of the next section.

5 Parallel Electron Heat Conduction

According to Eqn. 4, if the parallel power flow to the divertor plate is conduction-limited and the conductivity is given by the Spitzer-Härm value [4], i.e. Eqn. 1, then the temperature width is simply-related to the power width, i.e. $\lambda_T \approx 3.5\lambda_P$. This has been experimentally tested under conditions of low divertor radiation for Ohmic (deuterium), L-mode (hydrogen) and H-mode (deuterium, Type I ELMs) discharges, where the power width can be directly measured with IR thermography at the outer divertor plate, Fig. 3. The upstream λ_T is determined using ECE. An approximately constant ratio is obtained and is in reasonable agreement with the expectation, within the experimental error, which is estimated to be $\pm 25\%$

Fig. 4 illustrates the functional relation between the upstream temperature T_u at the nominal separatrix, as measured by (core) Thomson scattering, and the parallel power density. Again, low radiation (hydrogen) discharges are used so that $q_u \approx q_t$, where q_t is deduced from IR thermography at the outer plate. The line-average density was maintained fixed at $\overline{n}_e = 5.0 \times 10^{19} m^{-3}$, which gave a constant separatrix density of $n_u = 2.0 \times 10^{19} m^{-3}$, from lithium beam measurements. The power density was varied using NBI. The absolute error in the separatrix location at the mid-plane is $\approx 1cm$, and thus, with the large radial temperature gradients in the region, the absolute error in the T_u values is substantial (factor ≈ 2). However, the relative trends of the data are expected to be more accurate. In particular, the weak dependence of T_u on the power density is consistent with Eqn. 3, as illustrated in the figure, where $L = 25m$ has been used in this absolute calculation based on Spitzer-Härm [4]. The fact that large increases in parallel power q_u can be accommodated by a relatively small increase in temperature, and at constant density n_u, strongly suggests that parallel heat flux is determined by electron thermal conduction according to Spitzer-Härm conductivity.

These results, comparing the upstream conditions with the power at the plate, were obtained under low radiation conditions. Unfortunately, similar comparisons at high radiation levels, e.g. at high discharge density or with neon puffing, are not appropriate since divertor radiation modifies the magnitude and distribution of power incident on the plate. Under such conditions, we have only the upstream measurements to deduce features of the cross-field heat transport.

6 Plate Profiles vs Upstream Profiles

The effect of divertor radiation on the power distribution at the plate is illustrated in Fig. 5 for two Ohmic discharges, one at low density ($\overline{n}_e = 2.1 \times 10^{19} m^{-3}$, attached) and one at high density ($\overline{n}_e = 4.1 \times 10^{19} m^{-3}$, detached). Fig. 5a gives the parallel power density distribution at the outer plate, as inferred from IR thermography. At low density, radiation processes are negligible and the upstream power density q_u is

preserved down to the plate. The resulting q_t is highly peaked around the separatrix, having a characteristic width of $\lambda_P \approx 4mm$, which is approximately consistent with the upstream T_e profile, Fig. 5b, assuming that parallel power flow is determined by Spitzer-Härm electron conduction, i.e. the characteristic width of the T_e profile is $\lambda_T \approx 14mm$, roughly equal to $7/2\lambda_P$. (In this particular case, at low density, $T_u \gg T_t$ is not strictly satisfied and thus Eqn. 2 applies rather than Eqn. 3. If this complete expression is used, then the drop in separatrix temperature T_u at high density is consistent with constant q_u and Spitzer-Härm conduction.)

At high density, the separatrix power at the plate is reduced significantly, with little change further out in the SOL. Similar observations have been made on most divertor tokamaks [3, 15, 16, 17]. The profile appears to broaden significantly, in contrast with the upstream T_e profile, which shows no such broadening, Fig. 5b. The reduction of power near the separatrix appears to be balanced by impurity radiation processes in the divertor, as indicated by bolometer cameras, which preferentially favour regions close to the separatrix, particularly near the X-point region [18]. One possible explanation for this is the long connection length near the separatrix between the upstream power source and the divertor plate [3]. Thus, the evidence is consistent with no increase in λ_P, yet a significant broadening of the power profile on the plate.

Additional evidence supporting this scenario is obtained with the moving Langmuir probe, which gives plasma profiles below the X-point, but just above the recycling region close to the plate as shown in Fig. 1. At this location the plasma pressure loss along field lines, which is typical near plates under detached conditions, is not found [19]. Fig. 5c gives the electron pressure profile for the two densities, with similar characteristic widths ($\lambda_{pr} \approx 5mm$), comparable to that of the power deduced from IR thermography in the low density case. No broadening of the pressure profile at high density is observed, in contrast to the power measurement at the plate.

7 Dependence of λ_T on Discharge Parameters

In this section we summarize the behaviour of the upstream λ_T with respect to variations in P_{SOL} and line-average density $\overline{n}_e$, with the plasma current and toroidal magnetic field held within limited ranges, i.e. $0.8MA < I_p < 1.0MA$ and $2.0T < B_t < 2.5T$. P_{SOL} is the power entering the SOL, approximately determined using $P_{SOL} = P_{tot} - P_{rad,Xa}$, where P_{tot} is the total input power and $P_{rad,Xa}$ is the radiated power above the X-point.

The behaviour can be summarized very succinctly. The temperature e-folding width, as measured by ECE, is virtually independent of P_{SOL} and $\overline{n}_e$, and is simply described by $\lambda_T = 15mm \pm 5mm$. Fig. 6 illustrates this for a series of discharges, including Ohmic and L-mode density scans, and L and H-mode power scans. Very

similar results were obtained on ASDEX, with Thomson scattering [20]. In the case of the H-mode discharges, the profiles are averaged over ELMs, although profiles between ELMs differ little from the time-averaged profiles (see later). The approximately constant value for λ_T is consistent with the approximately constant power width $\lambda_P = 4mm \pm 1mm$ as determined from IR thermography in low radiation discharges (see next section).

8 Dependence of λ_P on Discharge Parameters

As with the temperature e-folding length, the power e-folding length λ_P as deduced from IR thermography (in discharges with low levels of radiation) shows only a weak variation over a large range of P_{SOL} and line-average density $\overline{n}_e$, again with the plasma current and toroidal magnetic field held within limited ranges, i.e. $0.8MA < I_p < 1.0MA$ and $2.0T < B_t < 2.5T$. Fig. 7 gives λ_P as a function of the parallel power density q_t at the outer plate (mapped to the outside mid-plane) for a number of Ohmic, L-mode and H-mode (Type I and Type III ELMs) discharges, with $P_{rad}/P_{tot} < 0.4$. As expected from the above λ_T measurements, the data is reasonably summarized by $\lambda_P = 4mm \pm 1mm$.

Within the present data set (Fig. 7), which consists of a collection of separate discharges obtained under a variety of machine conditions, no trend for λ_P with discharge parameters can be identified. However, in dedicated power scans in H-mode (Type I ELMy) discharges, a weak increase in λ_P with P_{SOL} is discernable, i.e. $\lambda_P \propto P_{SOL}^{1/2}$ [21]. Similarly, a dependence on safety factor q_{95} has been found [21], which is not observable in the present data set due to the limited range of plasma currents and magnetic fields.

9 ELMs: Time-Resolved Measurements

The H-mode boundary measurments presented above are averaged over ELMs, of either Type I or Type III. In this section we present ELM-resolved measurements (for Type I ELMs only), which demonstrate that the time-averaged measurements are virtually identical to inter-ELM profiles. We use for these measurments the edge Thomson scattering system, which samples at a frequency of 120 Hz. Although this is not sufficiently fast to resolve a single ELM, using averaging over a long series of identical ELMs, as is typical with Type I ELMs, time-resolved plasma profiles can be derived. A similar approach was used with earlier lithium beam measurements, which were compared and combined with fast ECE measurements to derive pressure profiles [22]. One advantage of Thomson scattering is that density and temperature are measured at the same time and location, thus eliminating errors associated with temporal or positional uncertainties that occur when the two quantities are

combined. The resulting pressure profile is therefore more accurate.

Fig. 8 gives electron density, temperature and pressure profiles so determined for an H-mode discharge (7978) in deuterium with $I_p = 1.2MA$,$B_t = 2.5T$, $\overline{n}_e = 7.5 \times 10^{19} m^{-3}$ and $P_{NBI} = 5.0MW$. The ELM frequency (Type I) was $\approx 100Hz$ and a $1s$ period has been used for averaging. Also included are the parallel power density profiles as determined at the outer plate using IR thermography. Profiles during two time periods are given in Fig. 8, both referenced with respect to the time at which the H_α signal in the divertor rises rapidly. The first time period, 0 ms to 1 ms, integrates over the ELM instability, which according to magnetic measurements occurs for $\approx 300\mu s$. The second time period, 8 ms to 9 ms, represents the typical 'between-ELM' profile, which, as we will demonstrate, is very similar to the time-averaged profile.

Immediately after the ELM event (0 ms to 1 ms), a quick flattening of the density and pressure profiles is seen, with a decrease in the main plasma and an increase further out in the SOL. The inversion radius for the profiles is the separatrix position, within experimental error. The broadening of the profiles disappears in a period $\approx 2ms$ (not shown). Qualitatively similar results were observed in the earlier study [22].

In the case of the T_e and q_t profiles, only a slight broadening is observed in the region in the SOL immediately adjacent to the separatrix. The close connection between the upstream temperature and the power at the plate, even during the ELM, is again consistent with electron heat conduction according to Spitzer-Härm. One should note that the parallel transit time for heat conduction is short, $\approx 100\mu s$, and thus the 1 ms effective integration time is not sufficiently fast to follow the heat pulse as it appears at the upstream location as an electron temperature pulse and at the plate as a surface temperature rise. This fast heat pulse is observable with both the ECE system at the mid-plane and the IR at the plate (not shown).

The pressure profile, Fig. 8c, indicates a rapid reduction in the pressure gradient at the boundary immediately following the ELM, which builds again until the next ELM. This time evolution is shown perhaps more clearly in Fig. 9, which gives the pressure gradient at $r = a - 1cm$ as a function of time during a single complete ELM cycle. For reference the divertor D_α behaviour is also given. One can see that the gradient builds during the inter-ELM period to a limiting value, consistent with the ideal ballooning limit, until it collapses again [22, 23, 24, 25]. The ideal ballooning limit for electrons at this radial location from magnetics (and assuming $T_i = T_e$) is $dp_e/dr \approx -200kPa/m$, based on a simple calculation for idealized geometry [26]. The error in the calculation is estimated to be approximately a factor 2.

The 're-building' time for the pressure gradient is $\approx 2ms$, which is roughly the transit time for ions to move along and across field lines in the affected region. The 'redistribution' of particles is also apparent in the H_α signal, Fig. 9a, which settles to a quasi-stationary value within $\approx 2ms$, following the start of the ELM event.

From Fig. 9b one can see there is little difference between the time-averaged and inter-ELM gradients. This illustrates the earlier claim that the time-averaged profiles are representative of the inter-ELM conditions.

10 Type I ELMs: Power Balance

In constrast to the situation in Ohmic and L-mode discharges, where power enters the SOL as a continuous stream (at least for time-scales $> 1ms$), in H-mode discharges, power enters the SOL in part as a continuous stream, but is regularly interrupted by ELMs, which introduce a discreteness into the power exhaust.

Fig. 10 summarizes the ELM contribution to the energy flow for a low radiation H-mode power scan in a single discharge (5583) with $I_p = 1.0MA$, $B_t = 2.5T$, $\overline{n}_e = 7 \times 10^{19} m^{-3}$ and varying NBI power [23]. From fast MHD measurements the energy exhausted per ELM is $\Delta E_{ELM} \approx 20kJ$, with a frequency f which increases in proportion to P_{SOL}. The corresponding energies which appear at the plates are relatively small, $\approx 2kJ$ at the outer plate and $\approx 5kJ$ at the inner, from IR measurments. The remaining energy, $\approx 13kJ$, is assumed to appear as radiation during the ELM, but cannot be time-resolved with the present bolometers on AUG. Fast spectroscopic measurements of impurity radiation are consistent with this hypothesis [27].

Fig. 11 gives the overall power balance (in a time-averaged sense) for this power scan, assuming that the missing ELM energy appears as radiation and is thus incorporated into the (slow) bolometer signals. Four components are given in the figure, corresponding to power either deposited on the two target plates or radiated either during ELMs or between ELMs (inter-ELM). The ELM contributions are determined using $P \equiv \Delta E f$.

In general, the input power is approximately accounted for to within an accuracy of $\pm 20\%$, with little variation with total input power in the relative share of the individual components. Of the total power added to the discharge, approximately 40% leaves the discharge in a discrete manner during ELMs, with the remainder leaving in a continuous stream between ELMs.

In the case of the continuous power loss between ELMs, radiative losses are comparable to the power deposited directly on the divertor plates. This is not the case during ELMs, where the radiative loss dominates the target power (as noted above). In fact, the time-averaged ELM power reaching the divertor plates is the smallest component in the power balance in this relatively low radiation discharge, comprising $\approx$ 12% of the total input power. Of this, the majority appears at the inner plate, Fig. 10b, with very little appearing at the outer plate.

The low level of the ELM power at the outer plate is illustrated more clearly in Fig. 12, which gives the spatial distribution of parallel power at the outer plate

(mapped to the mid-plane) in between ELMs, and time-averaged. Little difference is found between the two distributions, indicating that the dominant flow of power to the outer plate is the continuous stream between ELMs. Evidently, as mentioned above, radiation losses during the ELM shield the outer plate from most of the power exhausted from the main plasma during the discrete ELM event. The above results are consistent with a more extensive survey of ELMs on both ASDEX Upgrade and DIII-D [28].

11 Discussion

The primary result of this study is that the power e-folding width shows only a weak variation with discharge conditions in ASDEX Upgrade, and can be summarized by $\lambda_P = 4mm \pm 1mm$. (One should note that we refer here, as throughout the paper, only to the first power, temperature, pressure, etc., e-folding widths.) This includes Ohmic, L-mode and H-mode discharges, as well as a range of discharge densities, heating powers, fuel gases and machine conditions. A limited range of plasma currents and magnetic fields was explored. (The effect of safety factor is explored in [21].) In the case of H-mode discharges, this applies only to the time-average measurements, or equivalently inter-ELM conditions, since the profiles at the plates broaden somewhat during the ELM event itself, as shown in Sect. 9.

In the case of discharges with high levels of divertor radiation, λ_P can only be inferred from upstream T_e and plasma pressure measurements. These correspondingly show e-folding distances which are consistent with $\lambda_P = 4mm \pm 1mm$; that is, $\lambda_T = 15mm \pm 5mm$ and $\lambda_{pr} \approx 5mm$. While neither λ_T nor λ_{pr} are direct measures of λ_P, the simple modelling of Sects. 2 and 3 can be used to arrive at an approximate value.

The experimental evidence is consistent with parallel heat transport being determined by Spitzer-Härm electron heat conduction [4]. The evidence includes, (1) cases where λ_P and λ_T can be independently measured, giving values which are consistent with $\lambda_P = 2/7\lambda_T$ (Eqn. 4) (2) measurements of the functional dependence of the upstream temperature on parallel power density, which are close to the expected $T_u \propto q_u^{2/7}$ (Eqn. 3).

In H-mode discharges with Type I ELMs, the continuous stream of power crossing the separatrix between ELMs is strongly increased during these regular MHD events. The formation of a stochastic boundary on a short time-scale ($\approx 300\mu s$) results in a rapid exhaust of the heat content of the outer regions of the normally confined plasma. This heat, once it reaches the SOL, is rapidly transported along field lines by electron heat conduction in a time $\approx 100\mu s$. The resulting broadening in the T_e and q_t profiles is minor (Fig. 8). This is not the case for the density and pressure profiles, which broaden significantly and then evolve over a period of

$\approx 2ms$, as is also reflected in the H_α signal, Fig. 9. This 'redistribution' time for the particles is expected based on the particle transit time across and along field lines in the affected region. This implies, since the (Type I) ELM period is $\approx 10ms$ in these discharges, that time-averaged profiles are similar to inter-ELM profiles.

Fig. 9 gives the electron pressure gradient as a function of time through one complete Type I ELM cycle. One can see that the time-averaged gradient is close to the inter-ELM gradient. It is curious that the pressure gradient reaches its limiting value well before the onset of the next ELM (which occurs at $t = 12ms$ on this time-scale), i.e. why does the next ELM not occur at $t = 6ms$, when the electron pressure gradient has already reached its limiting value? Recalling that the ideal ballooning limit is related to total pressure gradient, one possible explanation is that the ion temperature profile (which is not measured) evolves over a longer time scale than the electron temperature profile. This highlights the need for ion temperature diagnostics with high spatial and temporal resolution.

Type I ELMs appear to exhaust an energy comparable to that flowing between ELMs. Nevertheless, the divertor plates are predominantly shielded from this ELM energy, particularly the outer divertor plate (see discharge 5583, Figs. 10, 11 and 12). This is true even in discharges with modest levels of total radiation in a time-averaged sense (i.e. $P_{rad}/P_{tot} < 50\%$). At the present time it is not clear where this energy goes, although impurity radiation in the plasma periphery and divertor are the most likely candidates. One possible reason for the enhanced level of radiation for ELM-exhausted power (radiation fraction $\approx 70\%$), compared with inter-ELM power (radiation fraction $\approx 45\%$), is related to the rapid onset of the ELM itself. This exposes impurities ions in the plasma periphery and divertor to elevated electron temperatures for short periods. Under such conditions the radiation rate for low-Z impurities can be considerably enhanced above coronal equilibrium values and even the elevated levels already present in the boundary during quiescent periods [29]. Thus, even with similar impurity concentrations, the fraction of power radiated during an ELM can be higher than between ELMs.

12 Conclusions/Future

Heat transport at the boundary of divertor tokamaks remains a critical issue. While we have addressed in this paper several of the outstanding questions, there remains large uncertainties and gaps in our understanding. For example, under conditions of high divertor radiation we must infer the power e-folding width λ_P from upstream temperature or pressure measurements. Use of measured λ_T values requires an assumption regarding the parallel transport of heat, while, use of λ_{pr} requires even further assumptions with respect to the simple modelling. One way of proceeding is to use computer codes to assist in the interpretation of the experimental results.

While the present measurements are consistent with parallel electron heat conduction according to Spitzer-Härm conductivity [4] in the first power width, there are still questions regarding the roles of convection and kinetic effects in the parallel heat transport. For example, further out in the SOL there are good reasons to expect that cross-field and parallel convection of power may play a role [5]. In addition, since kinetic effects seem to be able to perturb the electron distribution function in the divertor, making it difficult to derive the local T_e with Langmuir probes [30], the question naturally arises, are there conditions under which the heat transport itself is affected by kinetic effects?

While we have characterized the power widths λ_P observed in ASDEX Upgrade, we have not proceeded to derive cross-field transport coefficients, i.e. $\chi_\perp$ values. This is primarily due to uncertainty regarding the process determining the cross-field transport, i.e. conduction, convection or something else. We presently have evidence suggesting that the cross-field transport in the boundary is related to the global behaviour of the discharge and not necessarily to the local properties, or is perhaps strongly non-linear with local properties [25]. We thus refrain at this point from deriving $\chi_\perp$ values based on the widths presented here.

Considerable work remains to be done regarding heat (and particle) transport during and between ELMs. The nature of the stochastic region is important since this determines the source of power in the SOL during the ELM event itself. The subsequent evolution of the SOL probably consists of a quick exhaust of the thermal energy by parallel electron heat conduction, following by a redistribution of plasma and neutral particles. The latter is an inherently two-dimensional process, requiring the use of codes to unravel the important physics.

Acknowledgments

C. S. Pitcher is thankful for personal support during this study from the Max-Planck-Institut für Plasmaphysik and the Canadian Fusion Fuels Technology Project. This work is also supported by the U.S. Department of Energy Contract No. DE-AC02-78ET51013.

References

[1] G Janeschitz, K Borrass, G Federici et al, J Nucl Mat 220-222 (1995) 73
[2] H Zohm, Plas Phys Contr Fusion 38 (1996) 105
[3] C S Pitcher and P C Stangeby, Plas Phys Contr Fusion, in press
[4] L Spitzer and R Härm, Phys Rev 89 (1953) 977

[5] G P Maddison, P C Stangeby and C S Pitcher, Int Workshop on Theory of Fusion Plasmas, Varenna, August 1996
[6] P C Stangeby and G M McCracken, Nucl Fusion 30 (1990) 1225
[7] B LaBombard e al, Phys Plasmas 2 (1995) 2242
[8] W Köppendörfer et al, Plasma Phys and Contr Nucl Fusion Research (1992) IAEA-CN-56/A-2-3
[9] C S Pitcher et al EPS Conf on Plasm Phys and Contr Fusion (Lisbon) (1993) (European Physical Society)
[10] A Herrmann et al, Plasm Phys Control Fusion 37 (1995) 17
[11] N A Salmon, 18th Inter Conf on IR and Millimeter Waves, University of Colchester, England (1993)
[12] J Schweinzer et al, EPS Conf on Plasm Phys and Contr Fusion (Bournemouth) (1995) (European Physical Society)
[13] H Murmann et al, Rev Sci Instrum 63 (1992) 4941
[14] W Suttrop, A G Peeters et al, IPP Report, in preparation
[15] T W Petrie et al, Nucl Fusion (1996), in press
[16] G F Matthews et al, Plasma Phys and Contr Fusion 37 (1995) A227
[17] N Asakura et al, Plasma Physics and Control Nucl Fusion Research (1994) IAEA-CN-60/A-4-I-3
[18] C S Pitcher et al, J Nucl Mat 220-222 (1995) 213
[19] C S Pitcher et al, EPS Conf on Plasm Phys and Contr Fusion (Bournemouth) (1995) (European Physical Society)
[20] H Murmann and M Huang, Plas Phys Contr Fus 27 (1985) 103
[21] A Herrmann et al, EPS Conf on Plasm Phys and Contr Fusion (Kiev) (1996) (European Physical Society)
[22] W Suttrop et al, EPS Conf on Plasm Phys and Contr Fusion (Bournemouth) (1995) (European Physical Society)
[23] W Suttrop et al, IAEA H-mode Workshop Princeton, Plas Phys Contr Fusion 38 (1996) 1407
[24] W Suttrop et al, EPS Conf on Plasm Phys and Contr Fusion (Kiev) (1996) (European Physical Society)
[25] C S Pitcher et al, submitted Physics of Plasmas
[26] J W Connor, R J Hastie and J B Taylor, Phys Rev Lett 40 (1978) 396
[27] A R Field, K Büchl, C J Fuchs et al, EPS Conf on Plasm Phys and Contr Fusion (Lisbon) (1993) (European Physical Society) 4-6
[28] A W Leonard, W Suttrop et al, J Nucl Mat (proc of 12th Int Conf on PSI in Contr Fus Device, France (1996))
[29] D E Post, J Nucl Mat 220-222 (1995) 143
[30] R Chodura, Contrib Plas Physics 36 (1996) 61

Figure Captions

1. Poloidal cross-section of ASDEX Upgrade showing the location of boundary diagnostics used in this study.

2. Typical profiles of electron density, temperature, pressure and parallel power from two identical H-mode discharges (shots 7985, 7994) with $I_p = 1.0MA$,$B_t = 2.5T$, $\overline{n}_e = 8 \times 10^{19} m^{-3}$ and $P_{NBI} = 5.0MW$. All measurements are mapped to the outside midplane.

3. Ratio of upstream e-folding widths, electron temperature λ_T (from ECE) to parallel power density λ_P (from IR thermography, outer plate) in low radiation discharges as a function of parallel power density at the plate q_t.

4. Upstream electron temperature T_u from Thomson scattering as a function of parallel power density q_t from IR thermography (outer plate) in low radiation discharges (7808, 7810). Also shown is an absolute comparison based on Spitzer-Härm conductivity.

5. Comparison of (a) plate profiles of deposited power with (b) upstream measurements of T_e from ECE for low and high density Ohmic discharges (5944, 5946). Also shown in (c) are electron pressure profiles obtained with a moving Langmuir probe located mid-way between the plate and the X-point. (a) and (c) correspond to the outer divertor.

6. The temperature e-folding width λ_T (mapped to the mid-plane) from ECE measurements under a range of conditions.

7. The power e-folding width λ_P (mapped to the mid-plane) from IR thermography measurements at the outer plate in low radiation discharges.

8. ELM-resolved SOL profiles of electron density, temperature and pressure from Thomson scattering in a low radiation H-mode with Type I ELMs (shot 7978, $t = 2.5s$ to $t = 3.5s$). Also shown in (d) are the corresponding parallel power density profiles from IR thermography (outer plate).

9. The divertor H_α time behaviour and the corresponding electron pressure gradient derived from Thomson scattering at $r = a - 1cm$ for the same discharge as depicted in Fig. 8.

10. Energy loss due to Type I ELMs in a discharge (5583) with varying heating power: (a) the ELM frequency f (b) the energy exhausted (on average) per ELM from the plasma, E_{MHD}, and absorbed at the plates from thermography.

11. Power balance in a discharge (5583) with varying heating power and Type I ELMs. The fractions of radiated power, powers deposited on the plates, during or between (inter) ELMs.

12. Parallel power density from IR thermography at the outer plate between ELMs and time-averaged over ELMs (shot 5583).

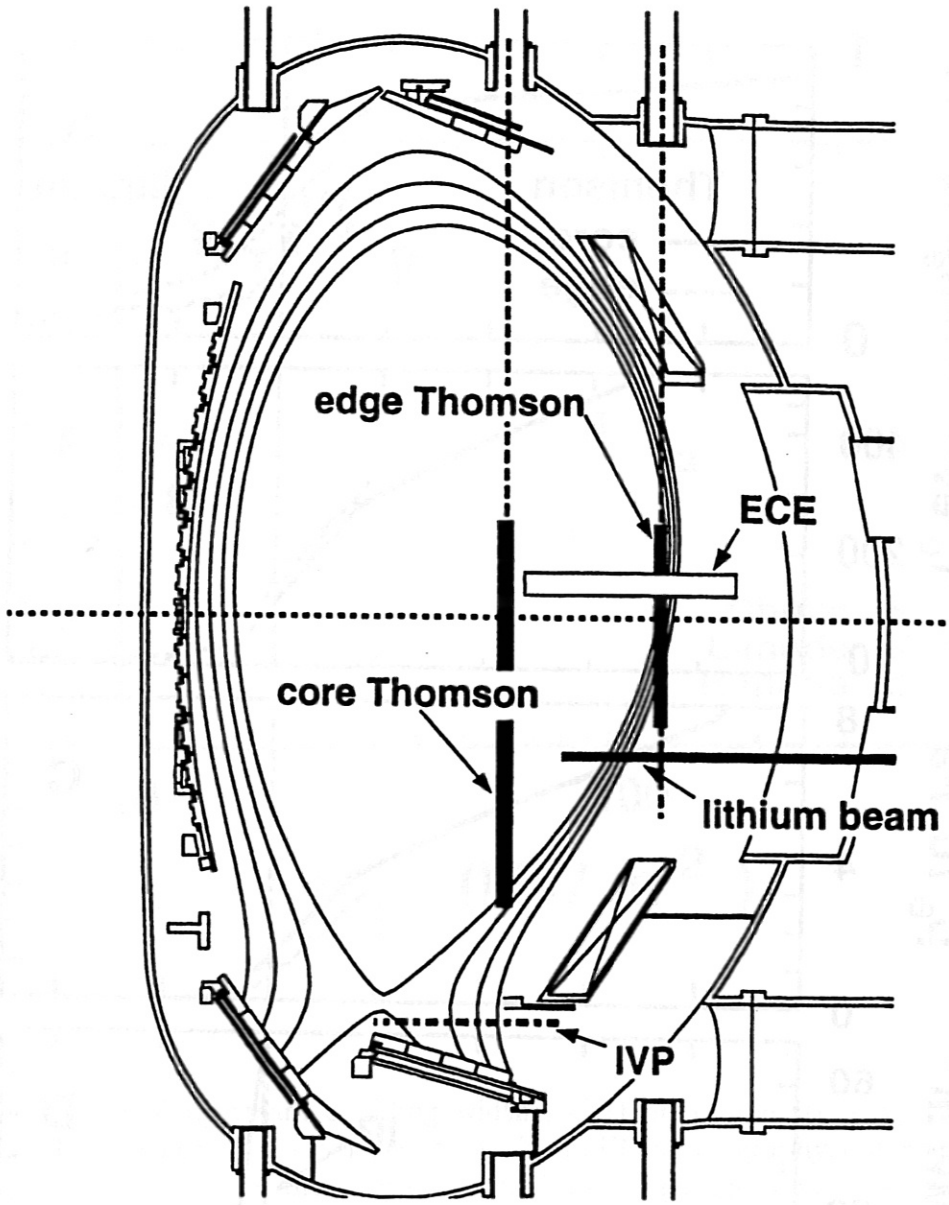

1. Poloidal cross-section of ASDEX Upgrade showing the location of boundary diagnostics used in this study.

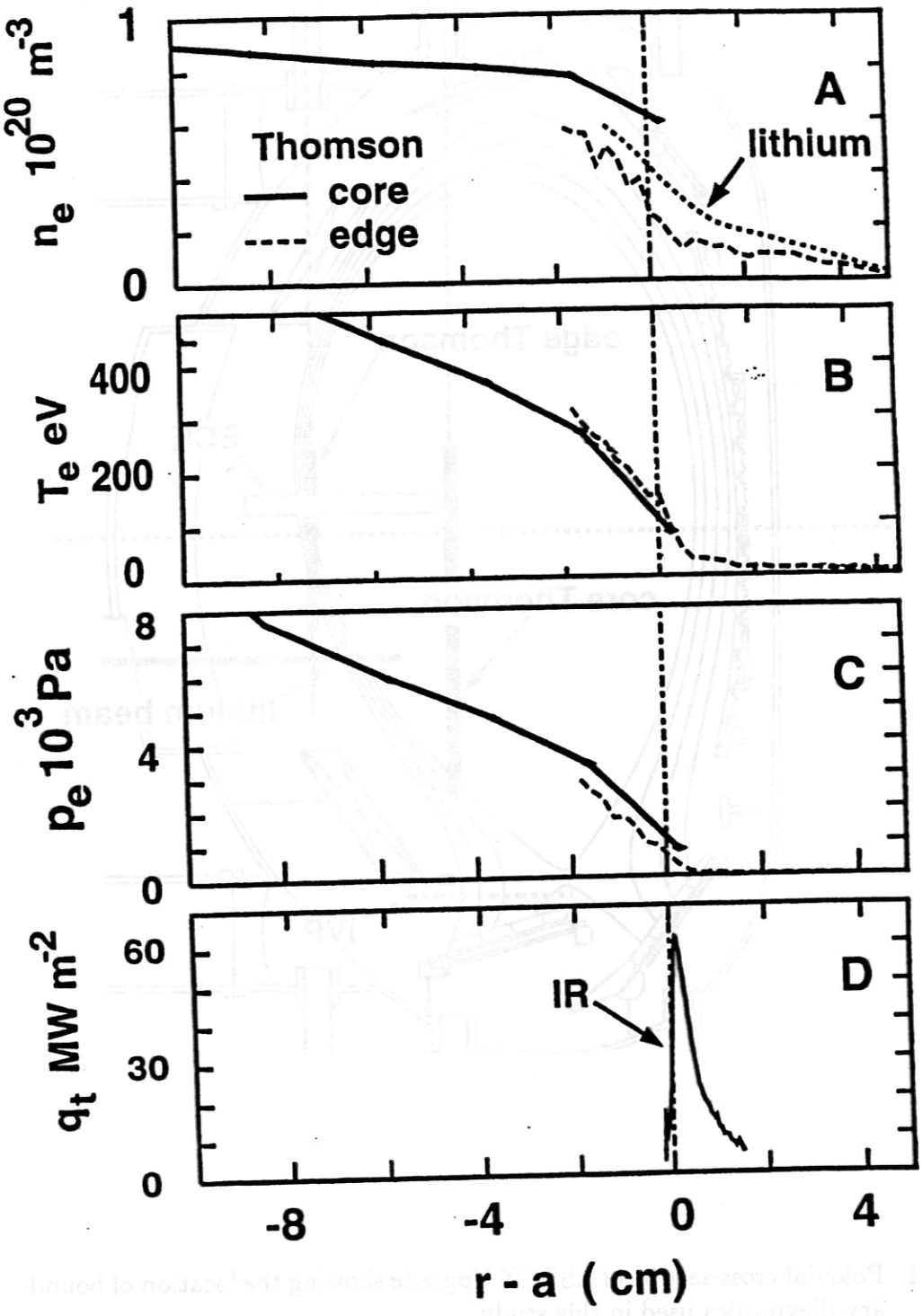

2. Typical profiles of electron density, temperature, pressure and parallel power from two identical H-mode discharges (shots 7985, 7994) with $I_p = 1.0MA, B_t = 2.5T$, $\overline{n}_e = 8 \times 10^{19} m^{-3}$ and $P_{NBI} = 5.0MW$. All measurements are mapped to the outside midplane.

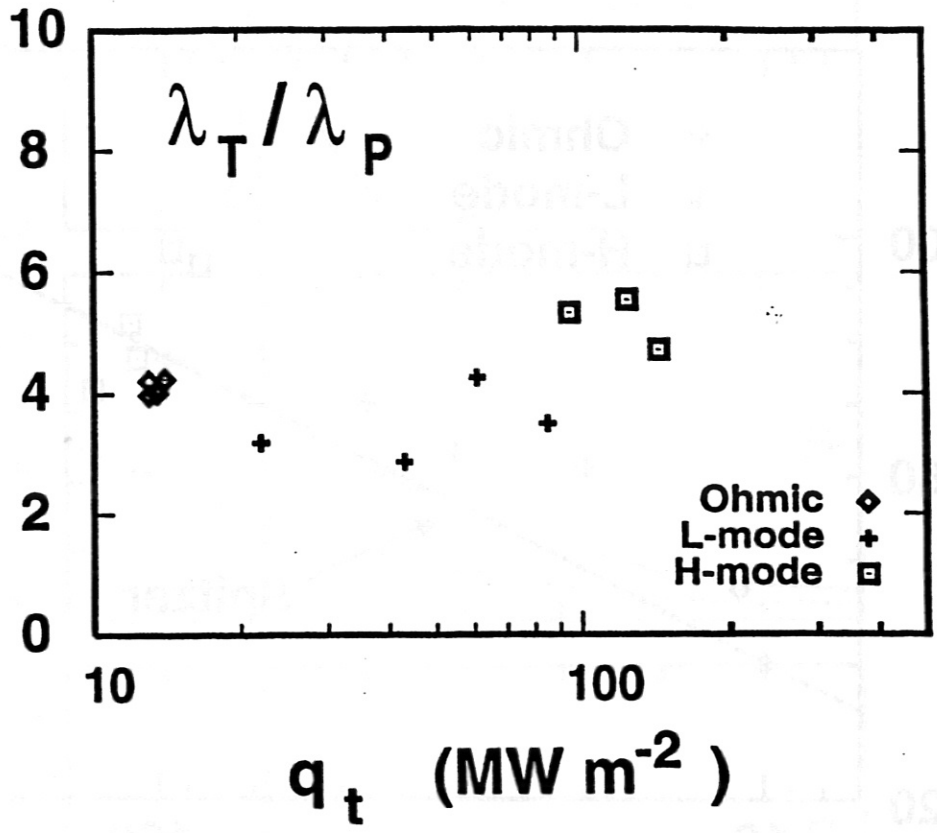

3. Ratio of upstream e-folding widths, electron temperature λ_T (from ECE) to parallel power density λ_P (from IR thermography, outer plate) in low radiation discharges as a function of parallel power density at the plate q_t.

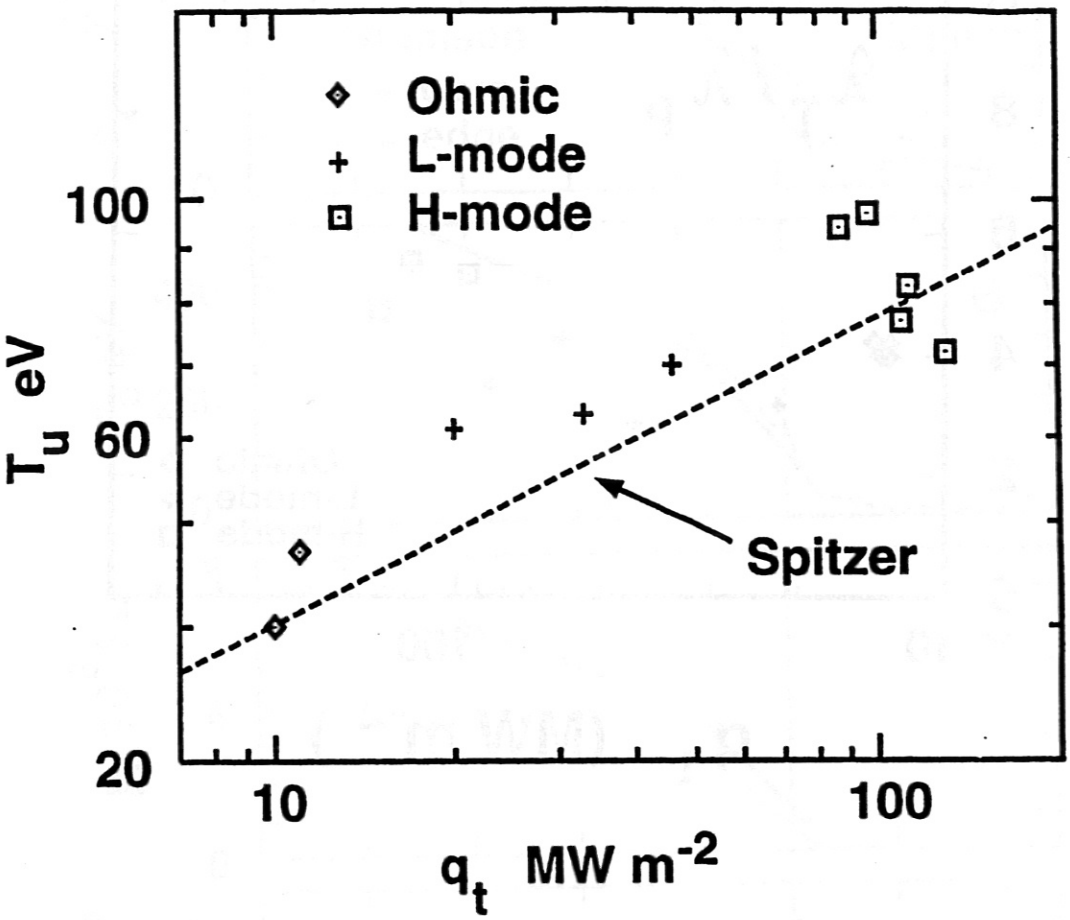

4. Upstream electron temperature T_u from Thomson scattering as a function of parallel power density q_t from IR thermography (outer plate) in low radiation discharges (7808, 7810). Also shown is an absolute comparison based on Spitzer-Härm conductivity.

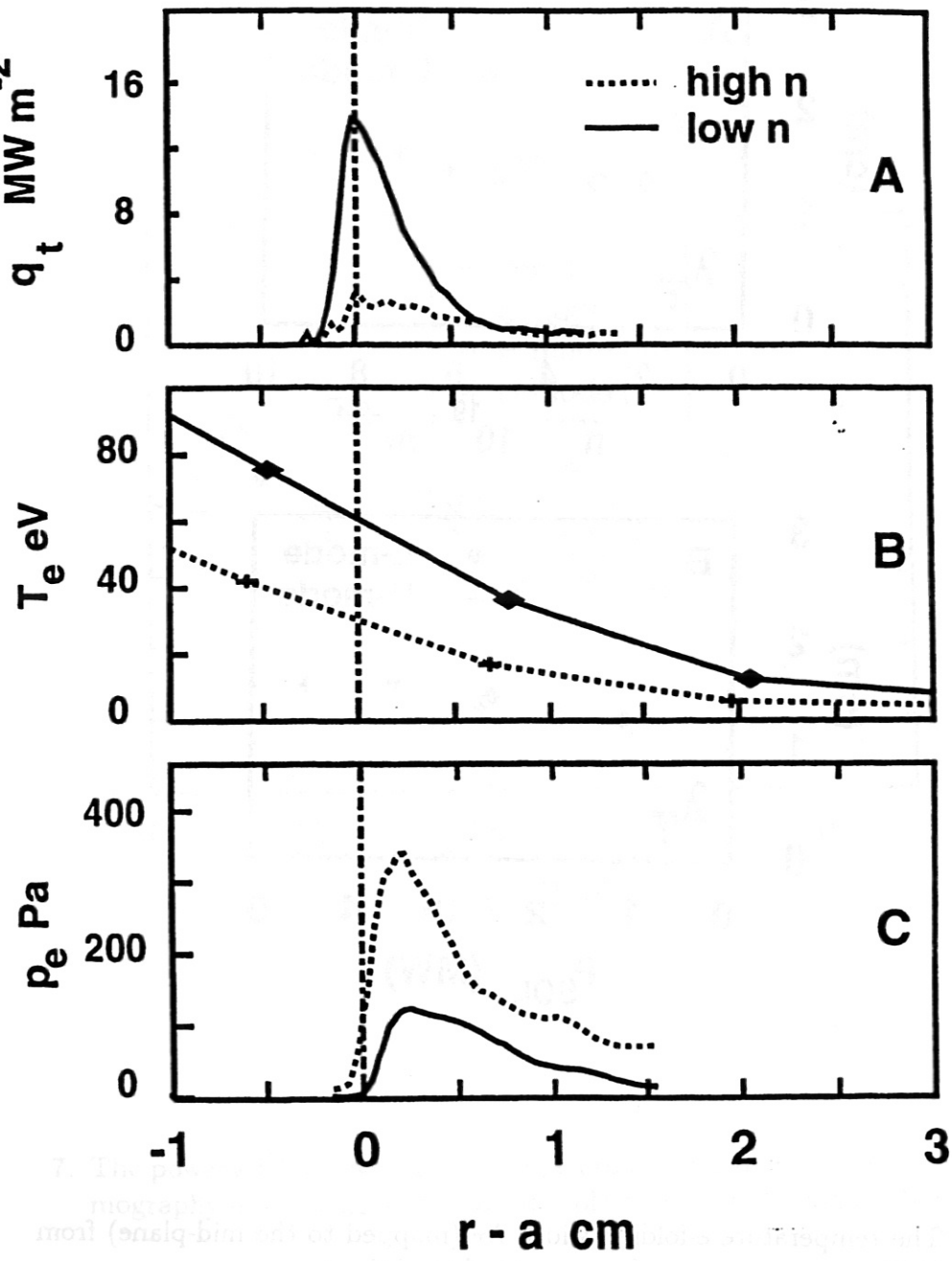

5. Comparison of (a) plate profiles of deposited power with (b) upstream measurements of T_e from ECE for low and high density Ohmic discharges (5944, 5946). Also shown in (c) are electron pressure profiles obtained with a moving Langmuir probe located mid-way between the plate and the X-point. (a) and (c) correspond to the outer divertor.

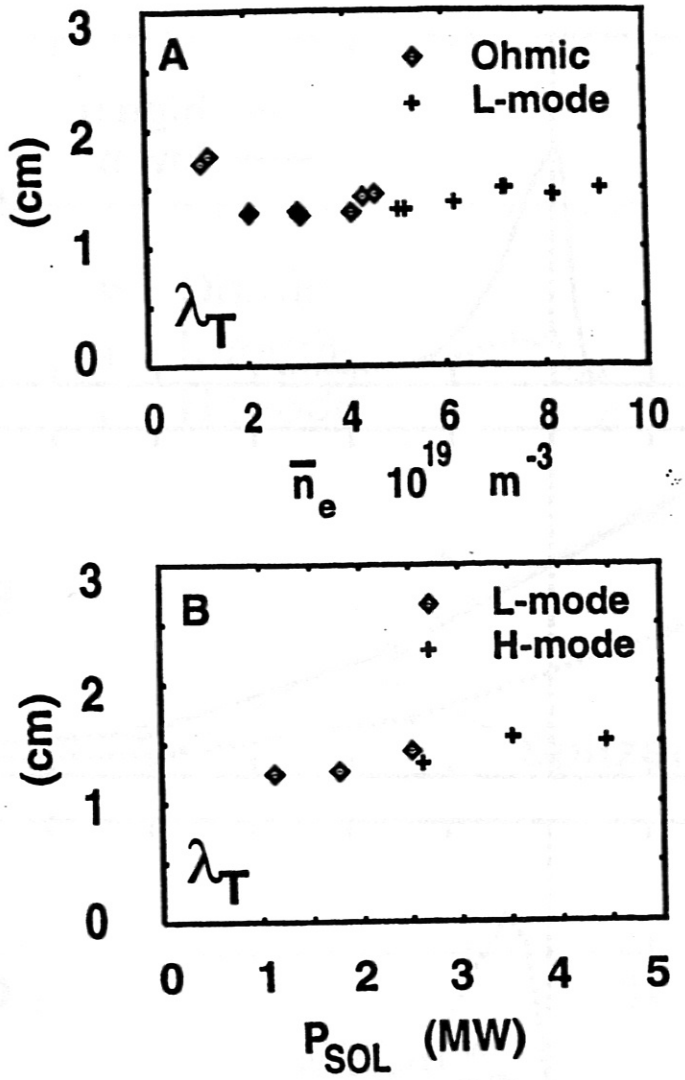

6. The temperature e-folding width λ_T (mapped to the mid-plane) from ECE measurements under a range of conditions.

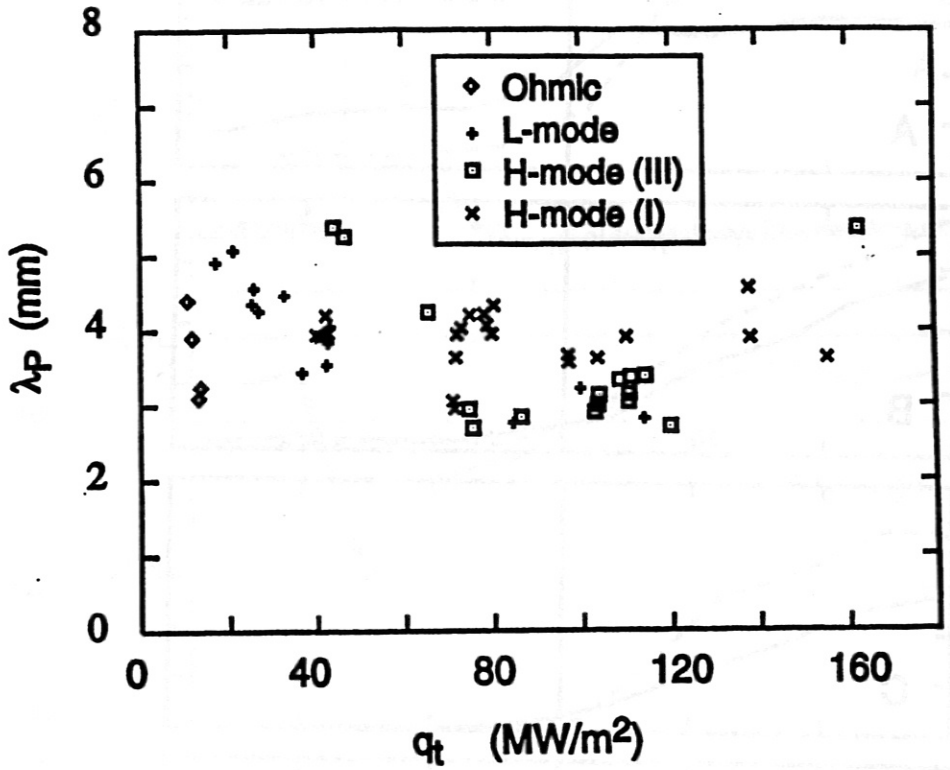

7. The power e-folding width λ_P (mapped to the mid-plane) from IR thermography measurements at the outer plate in low radiation discharges.

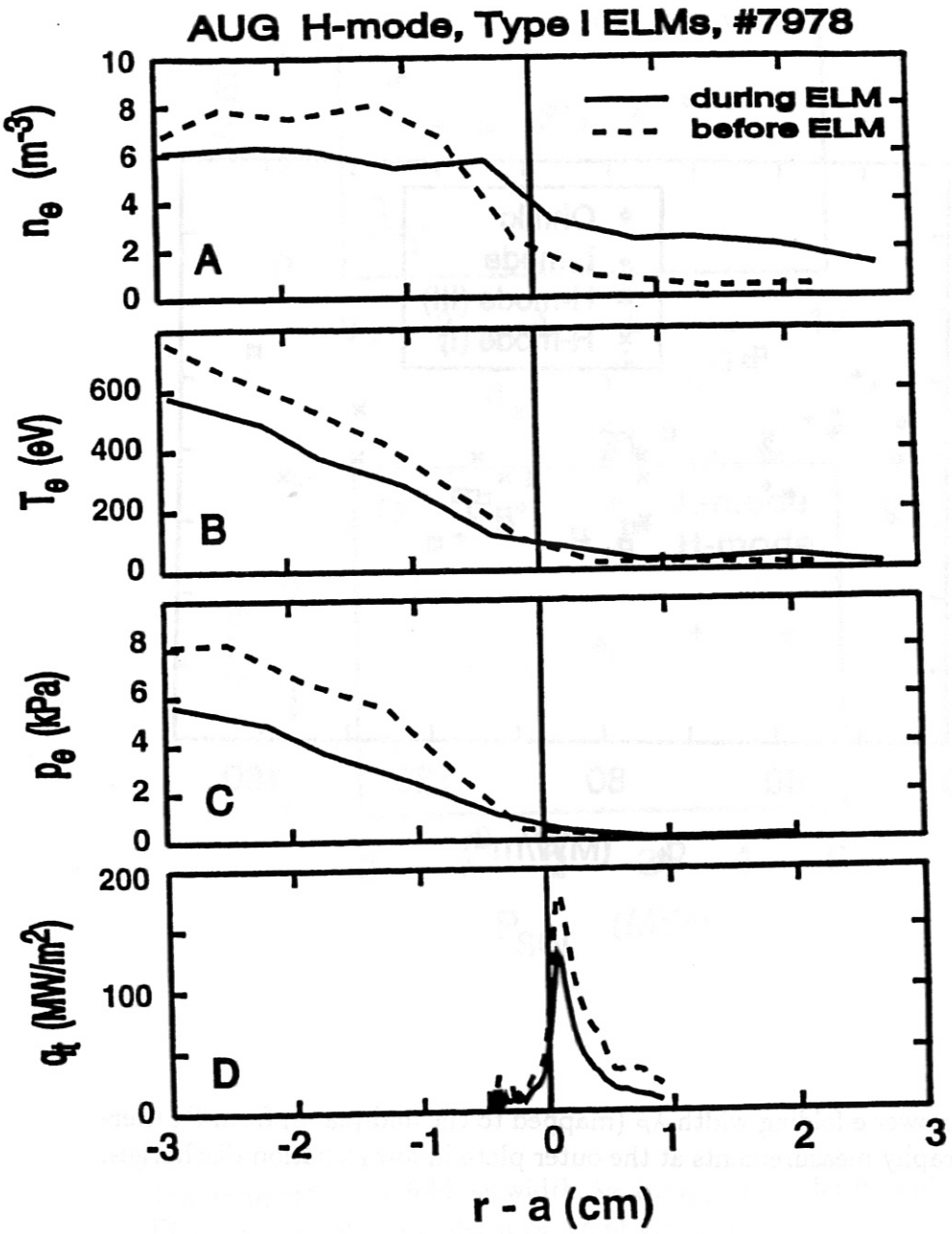

8. ELM-resolved SOL profiles of electron density, temperature and pressure from Thomson scattering in a low radiation H-mode with Type I ELMs (shot 7978, $t = 2.5s$ to $t = 3.5s$). Also shown in (d) are the corresponding parallel power density profiles from IR thermography (outer plate).

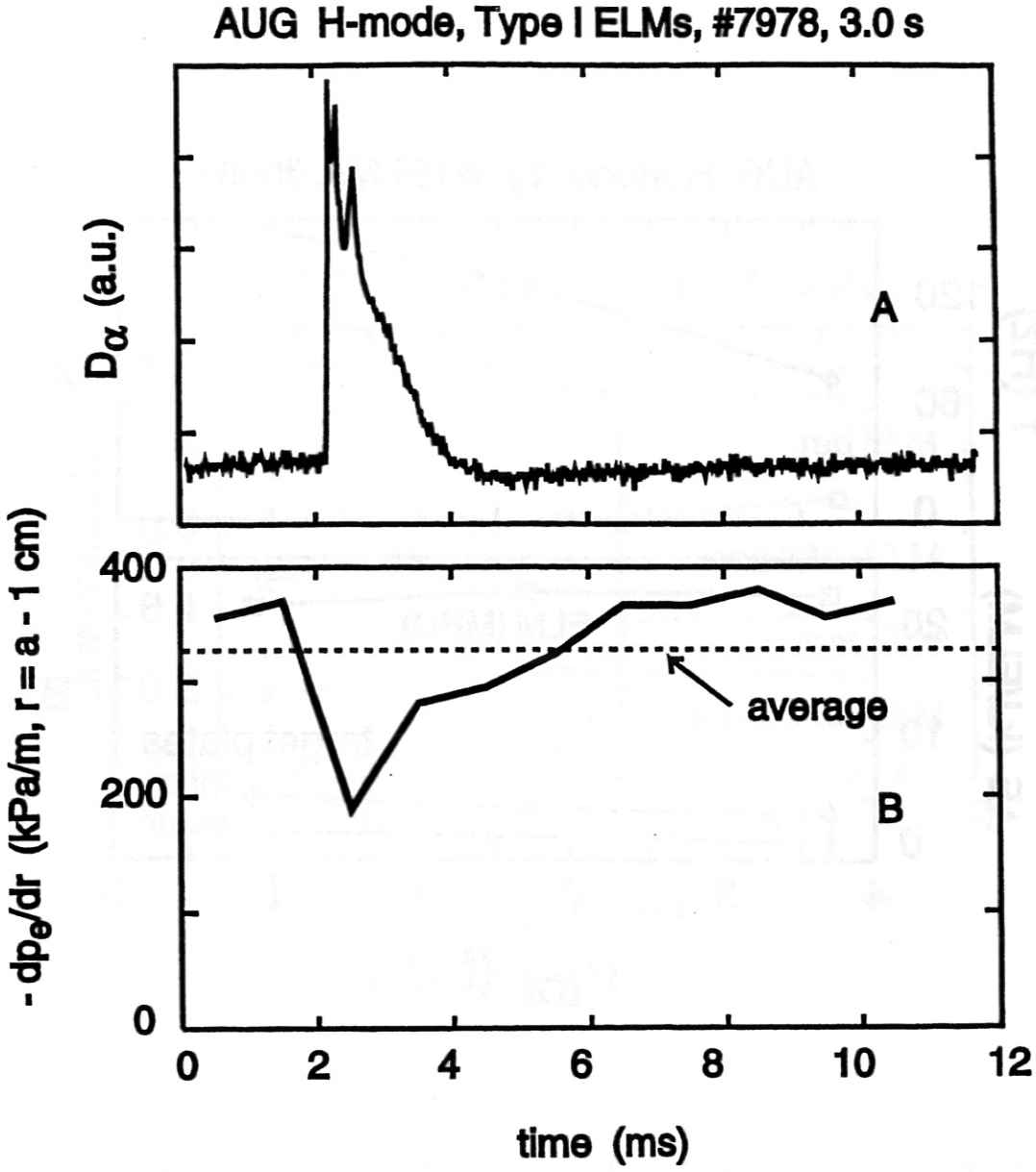

9. The divertor H_α time behaviour and the corresponding electron pressure gradient derived from Thomson scattering at $r = a - 1cm$ for the same discharge as depicted in Fig. 8.

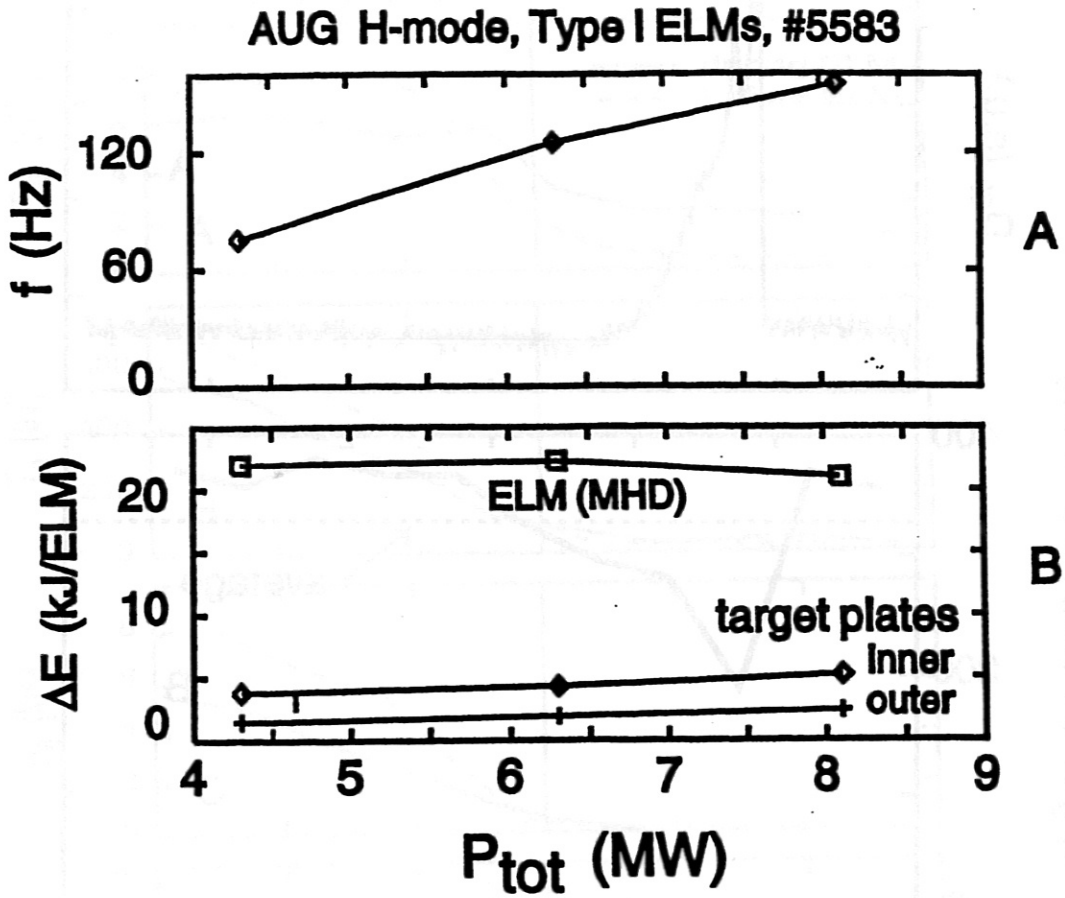

10. Energy loss due to Type I ELMs in a discharge (5583) with varying heating power: (a) the ELM frequency f (b) the energy exhausted (on average) per ELM from the plasma, E_{MHD}, and absorbed at the plates from thermography.

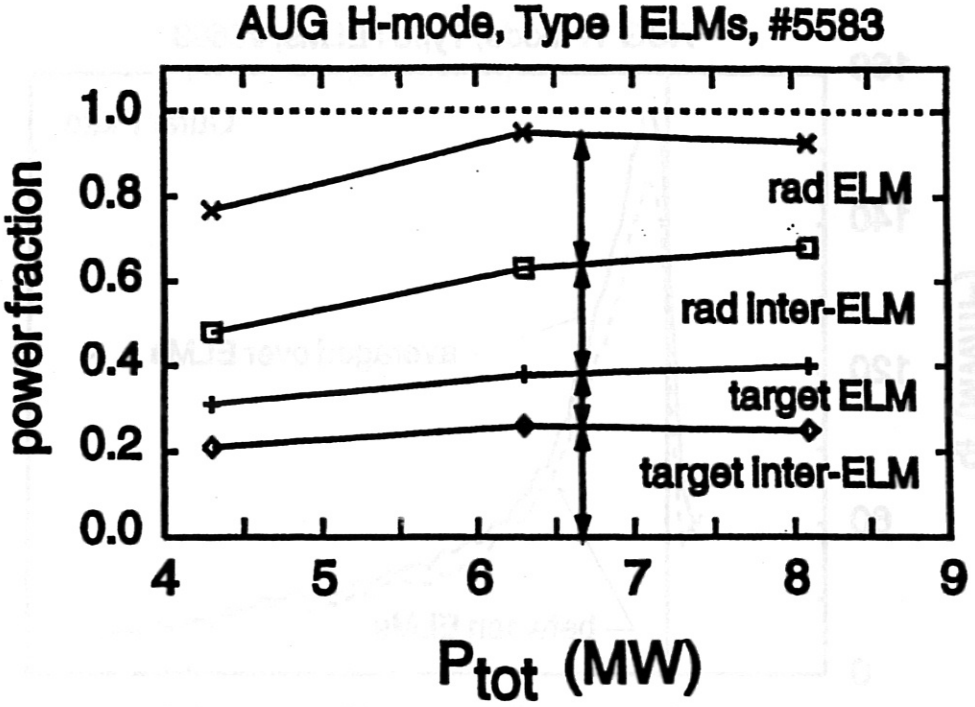

11. Power balance in a discharge (5583) with varying heating power and Type I ELMs. The fractions of radiated power, powers deposited on the plates, during or between (inter) ELMs.

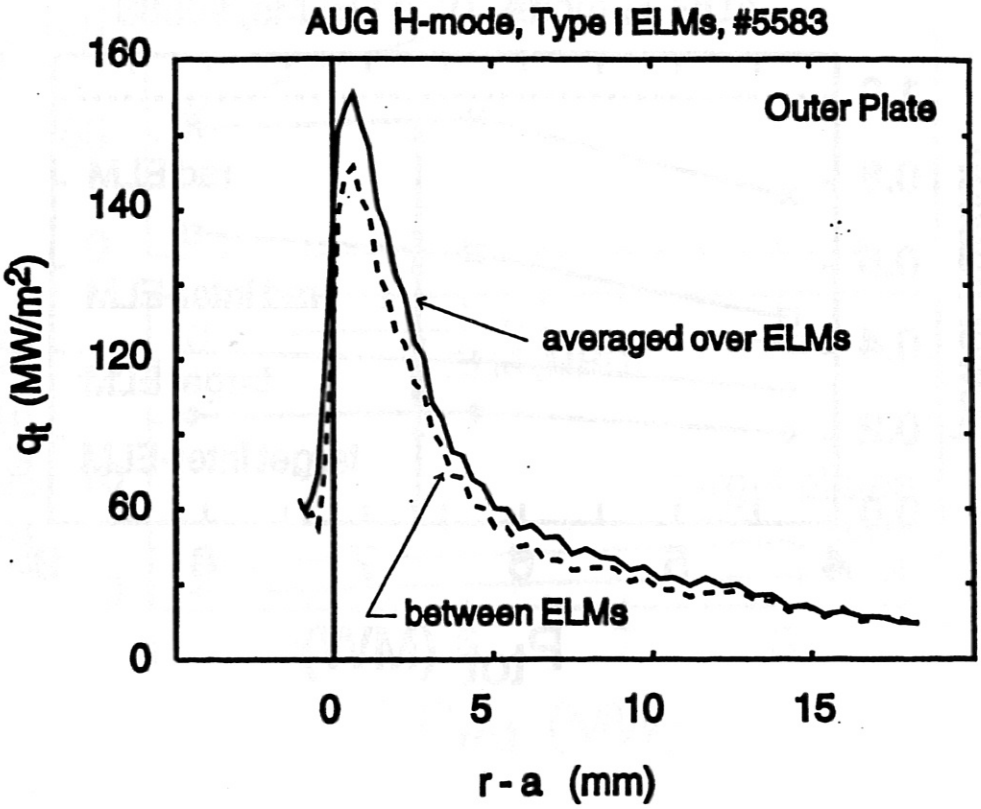

12. Parallel power density from IR thermography at the outer plate between ELMs and time-averaged over ELMs (shot 5583).